Object-based island green cover mapping by integrating UAV multispectral image and LiDAR data

Hao Liu,[a] Pengfeng Xiao,[a,b,*] Xueliang Zhang,[a] Xinghua Zhou,[c]
Jie Li,[c] and Rui Guo[a]
[a]Nanjing University, School of Geography and Ocean Science, Jiangsu Provincial
Key Laboratory of Geographic Information Science and Technology, Key Laboratory
for Land Satellite Remote Sensing Applications of Ministry of Natural Resources,
Nanjing, China
[b]Jiangsu Center for Collaborative Innovation in Geographical Information Resource
Development and Application, Nanjing, China
[c]The First Institute of Oceanography, Ministry of Natural Resources,
Marine Geomatics Center, Qingdao, China

Abstract. The unmanned aerial vehicle (UAV) plays an increasingly important role in monitoring and managing islands recently for their high feasibility and the miniaturization of sensors, which provide new possibilities for accurate island green cover mapping. We developed a framework that integrates UAV-acquired high-spatial resolution multispectral image and LiDAR data for effective object-based green cover mapping of Donkey Island in the Yellow Sea, China. LiDAR-derived structural and intensity information were combined with multispectral-derived spectral information for obtaining green cover objects. Five kinds of feature types [i.e., spectral, texture, height, intensity, and geometry features (GFs)] were calculated based on each object for green cover classification. Meanwhile, a multiple classifier system was adopted to improve the classification accuracy. The results indicate that the accuracy of green cover mapping could be significantly improved by the combination of multiple feature types. The inclusion of height and intensity features (IFs) can increase the overall classification accuracy by 7% and 5%, respectively, but the statistical significant differences are not found between these two feature types. The best green cover map is generated via a feature group obtained by the sequential backward selection with random forest method, reaching an overall accuracy of 88.5% and overall disagreement of 18.5%. Among the three major green cover classes, the accuracy of shrub class mapping improves the most when compared to classification using individual data, followed by tree and grass. Analysis of feature importance implies that spectral, height, and IFs are more beneficial to green cover mapping compared to texture and GFs. Furthermore, integrating multispectral and LiDAR data can provide more reliable green cover distribution maps and reduce the classification uncertainties. *© 2021 Society of Photo-Optical Instrumentation Engineers (SPIE)* [DOI: 10.1117/1.JRS.15.034512]

Keywords: Island green cover mapping; integration; object-based; unmanned aerial vehicle; multispectral; LiDAR.

Paper 210316 received May 15, 2021; accepted for publication Jul. 26, 2021; published online Aug. 10, 2021.

1 Introduction

With the intensification of island development activities, more attention is attached to the supervision of islands, especially the construction of the island ecological environment.[1] As the green space of the island, green cover plays crucial roles in purifying air, reducing noise, furnishing habitat for wildlife, beautifying island landscape, and improving residential property value.[2,3] Timely and accurate green cover mapping is of great significance for the ecological sustainability of islands.

---

*Address all correspondence to Pengfeng Xiao, xiaopf@nju.edu.cn

1931-3195/2021/$28.00 © 2021 SPIE

Recently, unmanned aerial vehicle (UAVs) remote sensing has shown great potential in identifying both the extent and the corresponding attributes of green cover,[4–6] performing more flexible, real-time, and cost-effective data acquisition compared to satellite or airborne remote sensing,[7,8] especially in small island areas bothered with frequent cloud contamination. Furthermore, affected by laws and regulations, UAVs usually fly in areas without human presence (non-urban areas) and where visual control is possible (open areas)—this led to an abundance of applications in island areas compared to others. As a critical component of a UAV-based remote sensing system, digital cameras, multispectral sensors, and light detection and ranging (LiDAR) sensors are increasingly used for green cover mapping applications.[9–12]

Among the various data acquired by different sensors, multispectral images have been recognized as the principal data and have been successfully applied for green cover mapping, owing to its ability to obtain spectral and spatial information of objects.[13–15] However, there are still some challenges of utilizing spectral properties in recognizing similar green cover types. For example, a higher intraspecies than interspecies leaf spectral variability provided a fuzzy spectral signal;[16] high structural similarities have weakened the utility of some features such as crown shape, size, and vegetation index;[17] and canopy illumination and shading effects influence the spectral response of objects.[18] These limitations result in a relatively low accuracy for green cover mapping.

In contrast to multispectral data, LiDAR can provide three-dimensional information of the land surface, some vertical features derived from LiDAR such as canopy height model (CHM), digital surface model (DSM) can greatly distinguish high green cover from low green cover.[19,20] In addition to the height information, intensity information is also beneficial for recognizing vegetation species, especially when used with other structural LiDAR-derived variables.[21] Moreover, LiDAR can avoid shadow problems caused by surface objects shielding each other.[22] Despite its advantages, LiDAR has coarse spectral resolution, generally covering a single spectral range in the near-infrared region.[23] Some surface objects such as three-dimensional morphology (e.g., grassland and open space) cannot be accurately recognized by LiDAR data.[24] Therefore, considering the advantages and limitations of multispectral and LiDAR data, the integration of two datasets appear to be an effective way to compensate for the shortcomings of each other.

Aside from the adopted data, the right choice of classification approaches is also decisive for successful green cover mapping. In general, green cover mapping is performed via pixel-based and object-based image analysis (OBIA) methods.[25,26] Previous studies that mapping green cover types have demonstrated that OBIA with high-spatial resolution (HR) remote sensing data was superior to pixel-based methods.[27–29] Many studies have also dedicated to integrating HR multispectral images and LiDAR data using OBIA method to improve the accuracy of urban green cover mapping. Their efforts focused on developing suitable segmentation methods,[30,31] comparing the performance of different machine learning classifiers,[32,33] and exploring the capability of multiple features.[34,35] In addition, multiple classifier system (MCS), which has been used in many land cover classification applications recently, was viewed as an effective means to utilize the advantages of different classifiers.[36] However, the applicability of integrating multispectral and LiDAR data for green cover mapping in island areas remain largely unknown.

Further studies are needed to explore the potential of the utilization of such new platforms (UAVs) for island green cover mapping. First, the effect of height or intensity information derived from LiDAR in the image segmentation procedure was usually not examined.[35,37] The knowledge to integrate these two UAV datasets for a segmentation task is still limited. Second, considering the high-spatial heterogeneity of islands, more valuable features from multispectral and LiDAR data are required for accurate green cover mapping. Also the high data dimensionality coming from the integration of different datasets should be considered,[38] as well as the classification uncertainty,[39,40] which is an additional accuracy measure that can be used to assess the spatial variation of the classification performances.

The aim of this study is to develop a framework that integrates UAV-acquired HR multispectral image and LiDAR data for effective object-based island green cover mapping. The specific objectives are as follows: (1) to generate optimal image objects based on multispectral and LiDAR data; (2) to evaluate different feature selection methods as well as the contribution of each feature to the classification; and (3) to investigate the improvement degree of classification accuracy using these complementary data and the impact of different input features on classification uncertainty.

2 Study Area and Dataset

2.1 *Study Area*

The study area is situated in Donkey Island of Qingdao City, Shandong Province, China. The area covered by UAV data is shown in the red polygon in Fig. 1. It is ∼1 km from the mainland, with an area of 0.3 km^2 and average elevation of 15 m. There is a variety of green spaces in this area, including natural forest land, protective forest, street trees, production nursery, and artificial lawn, which make the study area a representative region for island green cover mapping.

2.2 *UAV Data*

The multispectral images were acquired from a DJI M210 V2 multirotor UAV with the Parrot Sequoia sensor [Fig. 2(a)] on July 25, 2019, between 13:00 and 15:00 (minimizing the effect of shadows), and a total of 3446 images were obtained by the UAV multispectral remote sensing system. A multispectral sensor was fixed on a gimbal, pointing downward to guarantee aerial image quality, and equipped with a global positioning system (GPS) receiver capable of recording exact position of each image. The details of multispectral data are shown in Table 1.

We used a AS-300H laser sensor mounted on a DJI M600 PRO multirotor UAV to obtain LiDAR data [Fig. 2(b)]. The acquisition date was August 20, 2018. The flight height was 50 m, with clear weather and wind speed of 6 km/h. Basic parameters of LiDAR system were given in Table 2. Although multispectral acquisition time was inconsistent with the LiDAR data (about a year later), these two datasets were collected in the summer, and vegetation phenology was roughly the same and was not cut down during this time.

2.3 *Data Preprocessing*

The multispectral data were processed using software Pix4Dmapper v4.4.10. All the acquired high-quality images (3028 images) were mosaicked together to produce a digital orthophoto map (DOM) that covers a large area. First, images were aligned using GPS data and inertial measurement unit. Second, the aligned images were stitched together to build orthomosaic. Third, orthomosaic were georeferenced using nine ground control points (Fig. 1), which were

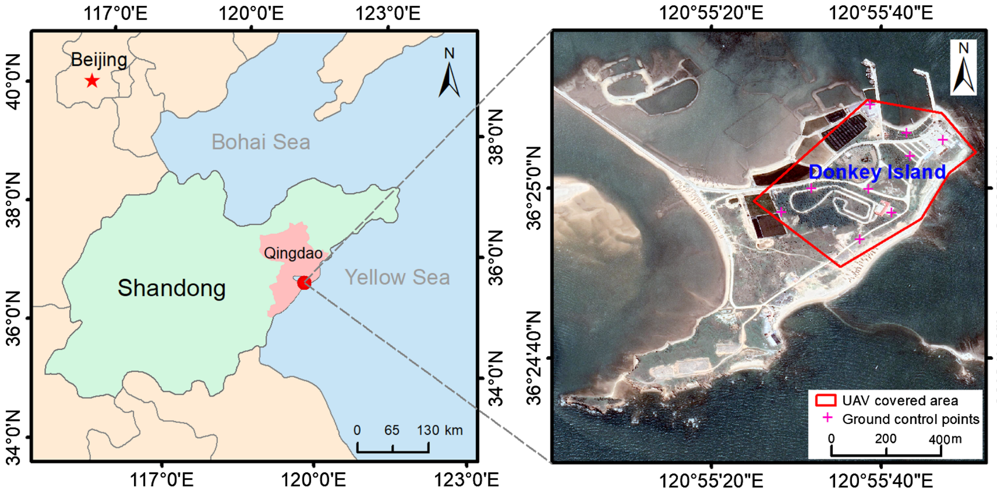

Fig. 1 Illustration of the study area in Donkey Island of Qingdao City, Shandong Province, China. The Landsat-8 image in the right plate was acquired on June 24, 2019, as shown with true color composite.

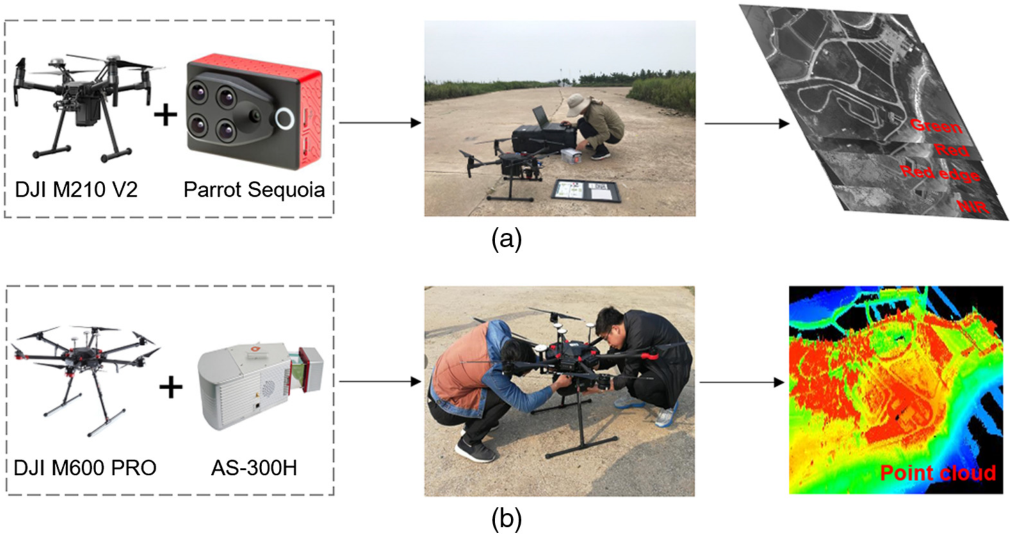

Fig. 2 Mapping devices used in this study: (a) multispectral system and (b) LiDAR system.

Table 1 Multispectral data collection information.

Parameter	Description
Weather	Sunny
Flight height	110 m
Forward/lateral overlap	80%/80%
Image resolution	1280 × 960 pixels
Spectral bands	G (550 nm, bandwidth 40 nm)
	R (660 nm, bandwidth 40 nm)
	RE (735 nm, bandwidth 10 nm)
	NIR (790 nm, bandwidth 40 nm)

Note: G: green; R: red; RE: red edge; and NIR: near-infrared.

Table 2 Basic parameters of the LiDAR system.

Parameter	Description
Wavelength	1024 nm
Scanning frequency	20 Hz
Measuring distance	250 m
Field of view	360 deg × 30 deg
Pulse emission frequency	100,000 point/s
Point density	30 point/m^2
Horizontal/vertical precision	5 cm/5 cm

measured by Trimble real-time GPS receiver in the field survey. The average root-mean-square error (RMSE) in the X, Y, and Z orientation of orthomosaic is 0.15 m. Finally, the conversion of the original gray value to the reflectance value was implemented based on a reference tile with known albedo values.

In order to combine with multispectral data and reduce the complexity of data processing, we transformed discrete LiDAR point clouds into two-dimensional raster data, including digital elevation model (DEM), DSM, CHM, and intensity image. Three general steps were implemented by software LiDAR360 V4.0: (1) the original point clouds were filtered (removing low, isolated, and air points); (2) the point clouds were classified into ground and non-ground points; and (3) the ground and all points were interpolated into DEM and DSM with 0.5 m resolution via the inversed distance weighting (IDW) algorithm (power is 2; search radius is 5 pixels; and nearest neighboring points are 12). The IDW was chosen based on the previous study, which proved that IDW was superior to a set of interpolation algorithms (e.g., ordinary Kriging, thin plate splines, and local polynomial) for producing elevation raster models from LiDAR data.[41] The CHM was created by subtracting DEM from DSM. Similarly, the point clouds (intensity data) were interpolated into an intensity image.

In this study, we used three datasets including multispectral DOM, CHM, and intensity image. Image registration was performed due to different spatial resolutions of the UAV data. The CHM and intensity image were resampled to the same pixel size as the multispectral DOM (0.12 m) using cubic convolution interpolation method since it can provide a good accuracy and is less geometrically distorted of the raster,[42] and the average RMSE in the X and Y orientation was 0.34 m. Subsequently, these three datasets were cropped to fit the study area, which ensured the consistency of spatial coverage (Fig. 3).

3 Methods

According to the green cover properties of the study area, we defined three green cover classes, i.e., tree, shrub, and grass. Figure 4 shows the designed workflow that integrates multispectral image and LiDAR data to accurately recognize three green cover types using an OBIA method. First, we segmented image objects from the multispectral and LiDAR data, followed by choosing the optimal segmentation scheme. Second, we calculated spectral, texture, height, intensity, and geometry feature (GF) values for each object, followed by selecting the optimal feature sets. Third, six feature groups were established (G1 to G6), which were used to analyze the impact of different feature types on green cover mapping. Finally, final green cover maps were generated using multiple classification system that contains three classifiers: support vector machine (SVM), k-nearest neighbor (KNN), and random forest (RF), and then the classification accuracy and classification uncertainty were assessed.

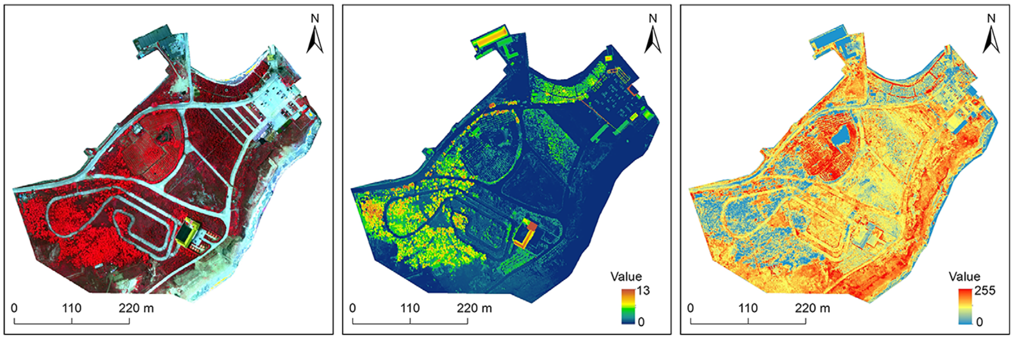

(a) (b) (c)

Fig. 3 Preprocessed images of multispectral and LiDAR data: (a) multispectral DOM (false color composite, red: near-infrared band, green: red band, and blue: green band), (b) CHM, and (c) intensity image.

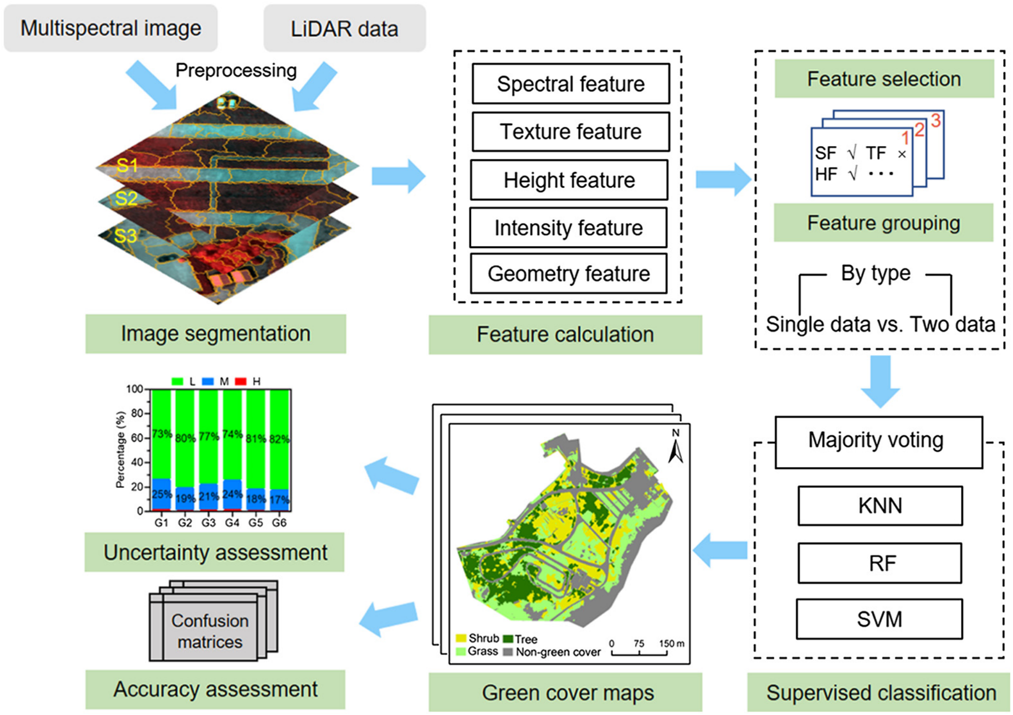

Fig. 4 Workflow of green cover mapping proposed in the study.

Table 3 Three segmentation schemes used to obtain image objects.

Segmentation scheme	Image layers
Multispectral-based (S1)	G, R, RE, and NIR
LiDAR-based (S2)	CHM and intensity image
Multispectral and LiDAR-based (S3)	G, R, RE, NIR, CHM, and intensity image

Note: G: green; R: red; RE: red edge; NIR: near-infrared; and CHM: canopy height model.

3.1 *Image Segmentation with Different Datasets*

We adopted the multiresolution segmentation (MRS) algorithm of Definiens eCognition Developer 9.0 to segment the images. This segmentation algorithm is a bottom-up region merging technique,[43] and the shape of image objects is controlled by two user-defined parameters: homogeneity (HOM) criteria and segmentation scale. The heterogeneity criteria comprise two pairs of indices: weights between shape/color and compactness/smoothness that control the allowed spectral or spatial degree of heterogeneity in each image object, where the total value of weight for each pair criterion is equal to one. Segmentation scale controls the number of image objects, where a lower value yields smaller and more homogeneous objects.

Three segmentation schemes were adopted to investigate the performance of different datasets on the segmentation results, i.e., multispectral-based segmentation (S1), LiDAR-based segmentation (S2), and multispectral and LiDAR-based segmentation (S3), as shown in Table 3. In MRS algorithm, scale is the most important factor influencing the segmentation results, therefore, we analyzed the scale parameter ranging from 20 to 250, with an increment of 10. Color and compactness parameters were set to 0.6 and 0.5 for each segmentation scale, respectively, since the spectral information needs more weight during the segmentation. The weights of the image layers were set to one for all bands to avoid any bias.

To obtain the optimal segmentation scale, an unsupervised segmentation evaluation method was utilized.[44] We calculated the overall “score” [standard deviation (SD)] for each image segmentation. SD can be defined as follows:

$$\mathrm{SD} = \frac{1}{lm}\sum_{k=1}^{l}\sum_{i=1}^{m}\mathrm{norm}(\mathrm{SD}_{ki}), \tag{1}$$

where SD_{ki} is the standard deviation of band k in segment i; m is the number of segments in the band; l is the number of bands in image layers; and norm refers to the min–max normalization. When SD is the largest, the corresponding segmentation scale is the optimal segmentation scale.

3.2 *Feature Calculation*

Following the image segmentation process, features can be calculated based on single- or multiple-input raster layers within an image object. We calculated a set of spectral features (SFs) and texture features (TFs) from multispectral data (Table 4). Four typical TFs were selected based on the previous studies using similar datasets,[45,46] which found that the GLCM entropy, GLCM homogeneity, GLCM angular second, and GLCM mean features are superior to other TFs in distinguishing vegetation from building and road. Furthermore, in order to reduce the feature redundancy, these four typical TFs were extracted from the first principal component after principal components analysis of the multispectral data.

In order to examine the use of LiDAR information for green cover classification task, four height and intensity features (IFs) were calculated based on LiDAR data. The detailed information of two types features was presented in Table 5.

Table 4 Spectral and TFs applied for green cover classification.

Feature type	ID	Description
SFs		
Mean: R, G, RE, and NIR	SF1 to SF4	Mean reflectance of all pixels in an object
SD: R, G, RE, and NIR	SF5 to SF8	Standard deviation of the reflectance of all pixels an object
Brightness	SF9	Mean value of $\mathrm{mean}_{\mathrm{R,G,RE,NIR}}$
Normalize differential vegetation index (NDVI)	SF10	$\mathrm{NDVI} = (\mathrm{NIR} - \mathrm{R})/(\mathrm{NIR} + \mathrm{R})$
Ratio vegetation index (RVI)	SF11	$\mathrm{RVI} = \mathrm{NIR}/\mathrm{R}$
Normalize differential water index (NDWI)	SF12	$\mathrm{NDWI} = (\mathrm{G} - \mathrm{NIR})/(\mathrm{G} + \mathrm{NIR})$
Red edge normalized difference vegetation index (RENDVI)	SF13	$\mathrm{RENDVI} = (\mathrm{NIR} - \mathrm{RE})/(\mathrm{NIR} + \mathrm{RE})$
TFs		
Homogeneity (HOM), entropy (ENT), mean (MEA), and angular second moment (ASM)	TF1 to TF4	Texture features based on the gray-level co-occurrence matrix in all directions

Note: G: green; R: red; RE: red edge; and NIR: near-infrared.

Table 5 Height and IFs applied for green cover classification.

Feature types	ID	Description
HFs		
SD H, min H, max H, and mean H	HF1 to HF4	Standard deviation, minimum value, maximum value, and mean value of an image object in the CHM
IFs		
SD I, min I, max I, and mean I	IF1 to IF4	Standard deviation, minimum value, maximum value, and mean value of an image object in the intensity image

Moreover, we extracted three GFs, containing length/width (GF1), area (GF2), and shape index (GF3). In this study, five different feature types were concerned, with a total of 28 features. Considering the numerical distribution of the five types of features was quite different, we utilized the Z-score method[47] to standardize all features data (including SFs, TFs, height features (HFs), IFs, and geometry features) prior to subsequent processing. The processed data (X) presented normally distributed with variance 1 and mean value 0. The calculation expression is as follows:

$$X = \frac{x - \mu}{\mathrm{SD}}, \tag{2}$$

where x is the raw data, μ is the mean value of the data, and SD is the standard deviation of the data.

3.3 *Feature Subset Selection*

Optimizing high-dimensional feature sets is an important step in green cover mapping since it can reduce redundant information and improve classification efficiency. Thus we adopted three classical feature selection methods in this study, including two filter methods (chi-square and correlation-based feature selection) and one wrapper method [sequential backward selection with random forest (SBS-RF)] to obtain the optimal feature subset. The Jeffries–Matusita (J–M) distance[48] was used to assess the performance of each feature selection method. The value of J–M distance is between 0 and $\sqrt{2}$, and its higher value indicates higher separability of the class pairs in the features. Each feature selection method is described as follows.

3.3.1 *Chi-square statistic*

Chi-square statistic (CHI) is a hypothesis testing method used to test the independence between variables.[49] For feature selection, CHI is used to evaluate the worth of a feature by calculating the chi-squared score of the classes and to obtain the rank list of all features. The CHI score of a feature can be calculated as

$$\chi^2 = \sum_{i=1}^{r} \sum_{j=1}^{c} \frac{(n_{ij} - \mu_{ij})}{(\mu_{ij})}, \tag{3}$$

where r is the number of the discrete intervals for the particular feature, c is the number of classes, n_{ij} denotes the sample number in the i'th interval for a feature, and μ_{ij} denotes the expected frequency of n_{ij}.

3.3.2 *Correlation-based feature selection*

Correlation-based feature selection (CFS) is a multivariate filter selection method, which evaluates the attributes of feature subsets using a heuristic evaluation function based on the correlation of features.[50] The measure of a subset is computed using the following equation:

$$\mathrm{Merit}_{sk} = \frac{k\mu_{\mathrm{cf}}}{\sqrt{k + k(k-1)\mu_{\mathrm{ff}}}}, \tag{4}$$

where Merit_{sk} is the evaluation of subset s containing k features; μ_{cf} is the average class–feature correlation; and μ_{ff} is the average feature–feature correlation.

3.3.3 *Sequential backward selection with random forest*

Unlike the above-mentioned two filter feature selection methods, the wrapper methods interact with the actual classification algorithm and are used to evaluate feature sets.[51] We adopted the SBS-RF method, and its specific steps were as follows: (1) calculate the feature importance of all variables based on an out-of-bag (OOB) error of RF algorithm;[52] (2) remove one feature variable with the least importance using the SBS searching strategy with successive iteration, and calculate the overall accuracy (OA); and (3) choose the feature variables set, in which the minimum variable number and the highest OA set is regarded as a final feature subset.

3.4 *Green Cover Classification Scheme*

3.4.1 *Feature grouping and sampling data*

In order to explore the classification level that could be obtained by different input features, a total of six feature groups were applied for classification based on the considered features (Table 6). G1 and G4 were designed to evaluate the performance of the multispectral image and LiDAR data, respectively. G2, G3, G4, and G6 were designed to explore the performance of combining multispectral image and LiDAR data, where G6 was used to assess the effect of feature optimization.

A stratified random sampling of image objects was implemented based on the optimal segmentation scale. Samples were visually checked using the HR multispectral image and Google Earth image, with a total of 400 samples were selected (100 per class). We used the majority class of the polygon to create the image object label, which means if a polygon contained more than 70% of the specific class.[53] The ratio of training and test samples was set to 1.

3.4.2 *Classification algorithm*

The use of some classical machine learning algorithms such as RF, SVM, and KNN has shown a good performance when applied to multispectral image classification.[36] Hence, we designed an MCS that combines the outputs of three machine learning classifiers (SVM, KNN, and RF) to acquire the final classification results. The description of each classifier is presented as follows.

Random forest. The RF is an ensemble classification method that uses a random method to conduct a forest, which consists of many mutually independent decision trees.[54] After using the training set to establish the forest, each decision tree in the forest judges the unlabeled sample and then predicts the unlabeled sample as the category that voted most frequently. Two primary parameters are required for setting in an RF classifier: the number of decision trees (T) and the number of the random subsets of features (N) to consider when splitting each node in a tree.

Support vector machine. The SVM is a non-parametric distribution supervised learning classifier that seeks the optimal separation hyperplane by minimizing the upper bound of classification error. The SVM classifier supports different kernel functions, e.g., radial basis function (RBF), linear, and sigmoid, among which the RBF shows superiority to other kernel functions for fused datasets.[19,55] Thus we chose the RBF in this study, and two parameters need to be determined: penalty parameter C and kernel parameter γ.

Table 6 Different feature groups used in the classification process.

Feature groups	Input features
G1	Spectral + texture + geometry
G2	Spectral + texture + height + geometry
G3	Spectral + texture + intensity + geometry
G4	Height + intensity + geometry
G5	Spectral + texture + height + intensity + geometry
G6	Feature sets obtained by the best feature selection method

K-nearest neighbor. The KNN is a flexibility and simplicity machine learning method that is to find a predetermined number of training samples closest to the new point and predict labels from these samples.[56] The closest K neighbors (K) is a small tunable parameter (i.e., 1, 2, 3, ...), which are found from the training set and then used to vote for the final prediction.

The parameters tuning for each classifier were accomplished via repeated fivefold cross validation based on the training dataset. In this study, considering the overfitting problem and computing time, the RF classifier used 200 trees and a value of sqrt (m) for N (m is the number of feature imported). As for SVM, we selected 10 candidate values for C were {0.25, 0.5, 1, 2, 4, 8, 16, 32, 64, 128} and those for γ were {1/32, 1/16, 1/8, 1/4, 1/2, 1, 2, 4, 8, 16}. The best C and γ were set to 2 and 1/32, respectively. For KNN classifier, we test K values range from 1 to 20 with a step of 1, and the best K was set to be 1.

Here the majority vote was used to combine the outputs from the individual classifiers, which means that the class that got the most votes is the category of the object to be classified. If three classifiers vote the different classes for an input image object, the image object will be assigned to a class with highest probability among the three classifiers. All classification procedures were implemented in Python V3.8.

3.4.3 *Accuracy assessment*

Several measures were adopted to assess the accuracy of object-based green cover classification, including the OA, user's accuracy (UA), producer's accuracy (PA), and $F1$-score (F). Considering the indicator of kappa coefficient are misleading and flawed for the practical applications in remote sensing,[57] we used overall disagreement (OD) instead of Kappa coefficient in accuracy analysis. The former three measures can be calculated by confusion matrix.[58] The OD is calculated by following equations:[57]

$$p_{ij} = \left(\frac{n_{ij}}{\sum_{j=1}^{J} n_{ij}}\right)\left(\frac{N_i}{\sum_{i=1}^{J} N_i}\right), \tag{5}$$

$$Q = \frac{1}{2}\sum_{g=1}^{J}\left|\left(\sum_{i=1}^{J} p_{ig}\right) - \left(\sum_{j=1}^{J} p_{gj}\right)\right|, \tag{6}$$

$$A = \sum_{g=1}^{J} \min\left[\left(\sum_{i=1}^{J} p_{ig}\right) - p_{gg}, \left(\sum_{j=1}^{J} p_{gj}\right) - p_{gg}\right], \tag{7}$$

$$\mathrm{OD} = Q + A, \tag{8}$$

where P_{ij} is estimated proportion of the land cover class in the classification and reference maps; J is the number of land cover classes; n_{ij} is the number of objects classified as class i and referenced as class j; N_i is the total number of class i in the classification map; Q and A are the overall quantity disagreement and the overall allocation disagreement, respectively; and OD is the overall disagreement calculated by the sum of Q and A. When the value of OD is large, the classification accuracy is poor.

The $F1$-score is the harmonic mean between UA and PA, which was defined as in Eq. (9) for each class i:

$$F_i = \frac{2 \times \mathrm{PA}_i \times \mathrm{UA}_i}{\mathrm{PA}_i + \mathrm{UA}_i}. \tag{9}$$

Moreover, we employed the McNermar's test[59] to assess the levels of statistical significant difference for all green cover classification accuracies. The McNermar's is a non-parametric test applied to confusion matrices that have a 2 × 2 dimension. This test is based on the standardized normal statistic. The test value Z can be calculated as

$$Z = \frac{|f_{12} - f_{21}|}{\sqrt{f_{12} + f_{21}}}, \tag{10}$$

where f_{12} and f_{21} represent the off-diagonal entries in the matrix. The difference between a pair of classifications was considered statistically significant at a confidence of 95% if the calculated Z is larger than 1.96.

4 Results

4.1 *Optimal Segmentation*

Twenty-four segmentation results were obtained for each segmentation scheme (S1, S2, and S3). Figure 5 shows the relationship between SD, segmentation scale, and the number of image objects. It can be seen that the number of image objects decreases with increasing segmentation scale, and the changes of SD in different segmentation schemes are different to some extent. For both S1 and S3, SD increases with the increase of scale until a maximum is reaches. Conversely, SD in S2 decreases with the increase of scale until a minimum is achieves. Based on the evaluation method, the optimal segmentation scale for each segmentation scheme is determined at 80, 200, and 60, respectively, and the corresponding number of image objects is 2522, 307, and 4094, respectively.

According to the visual examination of the optimal segmentation results from each scheme (Fig. 5), image objects from S1 and S3 match better with the ground green cover objects. For S2, only intensity and height layers is used, leading to a large number of mixed segments, which makes it difficult to distinguish the boundaries of different land cover classes (such as grass and cement road).

To illustrate segmentation results of S1 and S3 in detail, zoomed-in subsets of three typical areas are separately shown in Fig. 6, including grass area (R1), shrub area (R2), and the mixed area of three green cover types (R3). On the whole, segmentation scheme S3 created better segmentation results than S1, especially in area R2 and R3. Specifically, S1 is not able to produce objects whose boundaries correspond to those of the various shapes shrubs (blue circles) in area R2. Similarly, some mixed image objects emerge that contain grass and shrubs (yellow squares) for area R3, and the boundaries of some grass objects are relatively broken (yellow circles). This can be attributed to fact that the S3 considers the role of height and intensity information that enhance the contrast among different green cover types. Hence, we adopted S3 as the final segmentation scheme to obtain the green cover objects.

4.2 *Optimal Feature Subset and Feature Importance*

The results of optimal feature set using three feature selection methods are presented in Table 7. Three methods (CHI, CFS, and SBS-RF) have good performances on the dimension reduction of feature subset, and the features reduction rate are 64.2%, 46.4%, and 78.5%, respectively. In terms of the separability among green cover types, the highest mean for *J–M* distance is achieved by SBS-RF method, followed by CHI and CFS. Regarding the three optimal feature subsets, the proportion of SFs is the highest, while the shape features is the lowest. Furthermore, it is worth noting that nine features (SF3, SF8, SF10, SF11, SF12, HF1, HF2, TF2, and IF3) are selected by at least two methods, which suggest that these features are beneficial to green cover mapping. Therefore, it is evident that SBS-RF is an appropriate feature selection method for green cover classification compared to both CHI and CFS methods.

Furthermore, to gain insight into the contribution of each input feature, feature importance analysis was performed based on the OOB error of RF algorithm. In addition to assessing the importance of each feature to overall classification accuracy, the importance of each feature to per green cover class was also assessed (Fig. 7).

The feature importance for all classes and per-class differs to a large extent. Concretely, high importance values for all classes are focused on spectral, height, and IFs, and the proportion is 7/10, 2/10, and 1/10, respectively, in the top 10 features [Fig. 7(a)]. For the tree class [Fig. 7(b)],

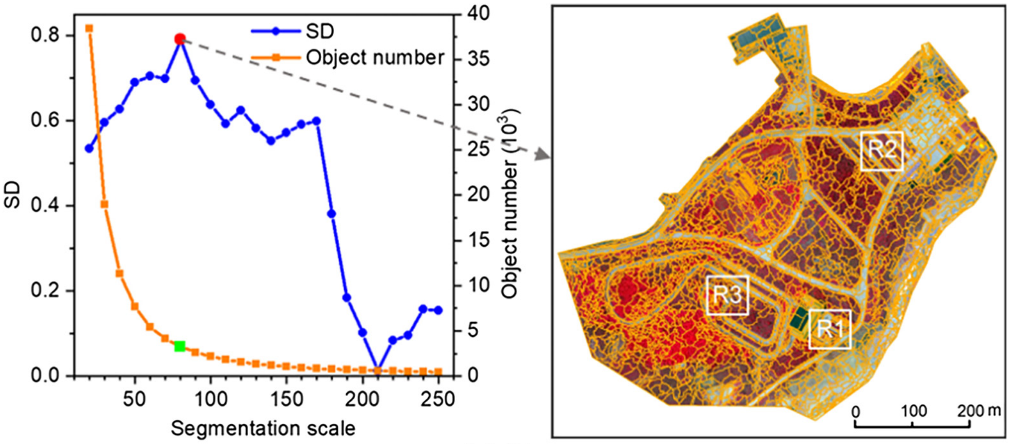

(a) S1

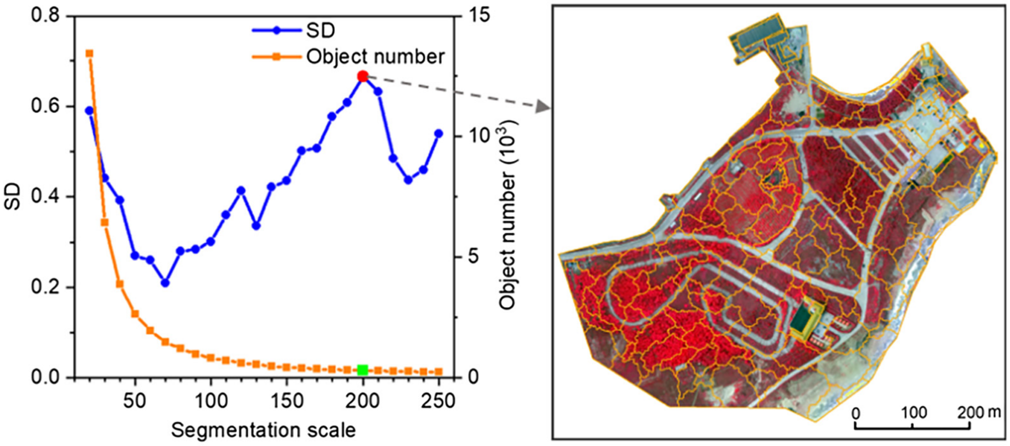

(b) S2

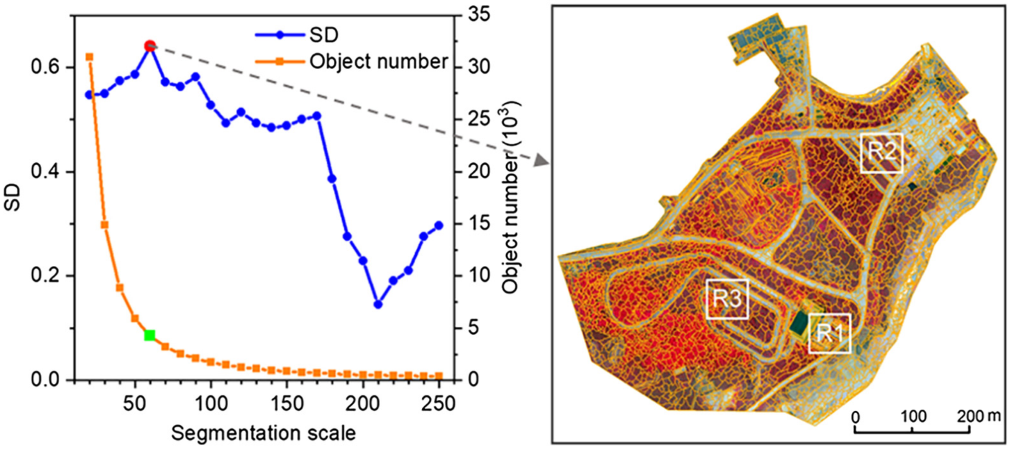

(c) S3

Fig. 5 Changes of SD and object number with scale parameter and the optimal segmentation results of three segmentation schemes: (a) S1, (b) S2, and (c) S3.

the min I extracted from the intensity data is the most important feature to discriminate the tree class, and the proportion of HFs increase (from 2/10 to 4/10), with the decreasing of the SFs proportion (from 7/10 to 5/10). For the shrub class [Fig. 7(c)], the texture and geometric features appears more important and they rank higher. For the grass class [Fig. 7(d)], the importance of texture, height, and IFs increased, especially the TF MEA is the second most important feature.

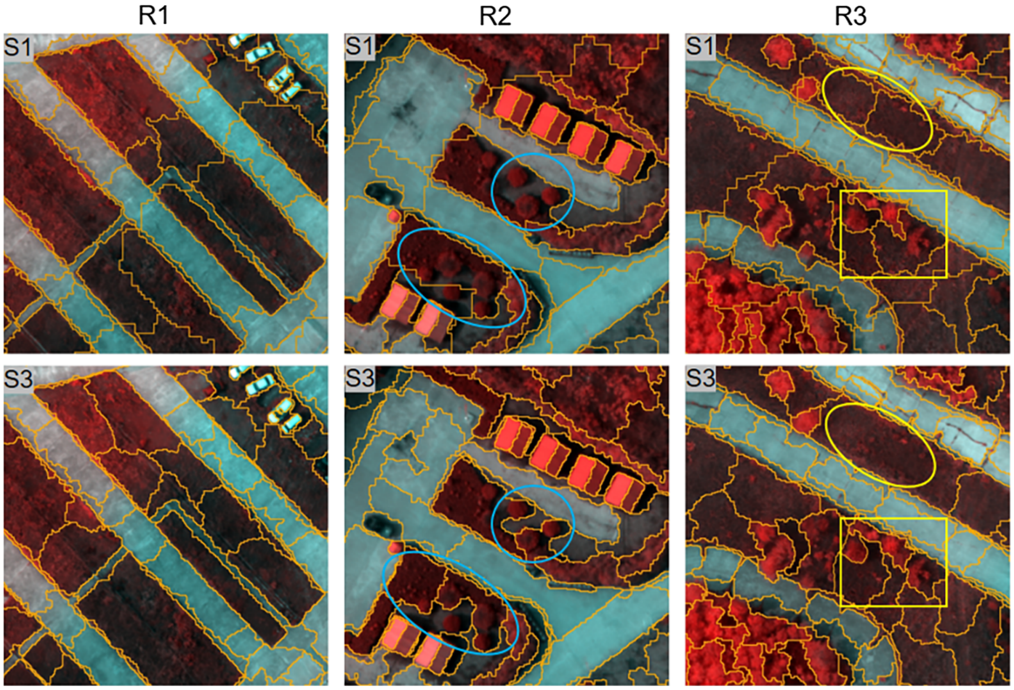

Fig. 6 Comparison of local segmentation performance of S1 and S3 in three typical green cover subareas R1, R2, and R3.

Table 7 Optimal feature subsets obtained by different feature selection methods. The features selected by at least two methods are highlighted in bold.

Methods	Feature sets	Number	Mean *J–M* distance
CHI	SF2, **SF8**, **SF10**, **SF11**, **SF12**, **HF1**, **HF2**, HF3, and **IF3**	9	1.414
CFS	SF1, **SF3**, SF5, SF7, **SF8**, **SF10**, **SF11**, **SF12**, **HF1**, **HF2**, HF4, **TF2**, TF3, IF2, and GF1	15	1.413
SBS-RF	**SF3**, **SF6**, **SF10**, TF2, **HF2**, and **IF3**	6	1.414

4.3 *Classification Accuracy*

The green cover maps of six feature groups (G1 to G6) produced by using MCS are shown in Fig. 8. Generally, it can be observed that these maps were consistent with the mostly distribution of ground green cover. A considerable improvement in green cover class confusion is seen in trees and shrubs (e.g., red circle), especially when both height and IFs are included (e.g., G5 and G6).

The OA and OD for each feature group suggest that the feature groups based on both multispectral image and LiDAR data can provide significantly better quality than those based on single data (Table 8). Specifically, the best OA is achieved with G6 including the features selected by SBS-RF method, and the best OD is achieved with G2 and G4. The poor classification performances are G1 and G4 that contain the single data (multispectral image or LiDAR data). Compared to G1, the inclusion of HFs (G2) and IFs (G3) to the classification yields a significant improvement in OA/OD: 7%/8% and 5.5%/6.5%, respectively. Meanwhile, feature optimization is helpful for improving the OA, while it is not effective for OD (G5 versus G6).

It can be noticed that the inclusion of height and IFs lead to a marked increase in UA and PA for three green cover classes [Fig. 9(a)], resulting in an increase of 8% and 12% for tree, 20% and 12% for shrub, and 2% and 9% for grass, respectively. The UA and PA for tree and grass are over 80% in all feature groups except G1 and G4, whereas the shrub of UA (mean of 70%) and

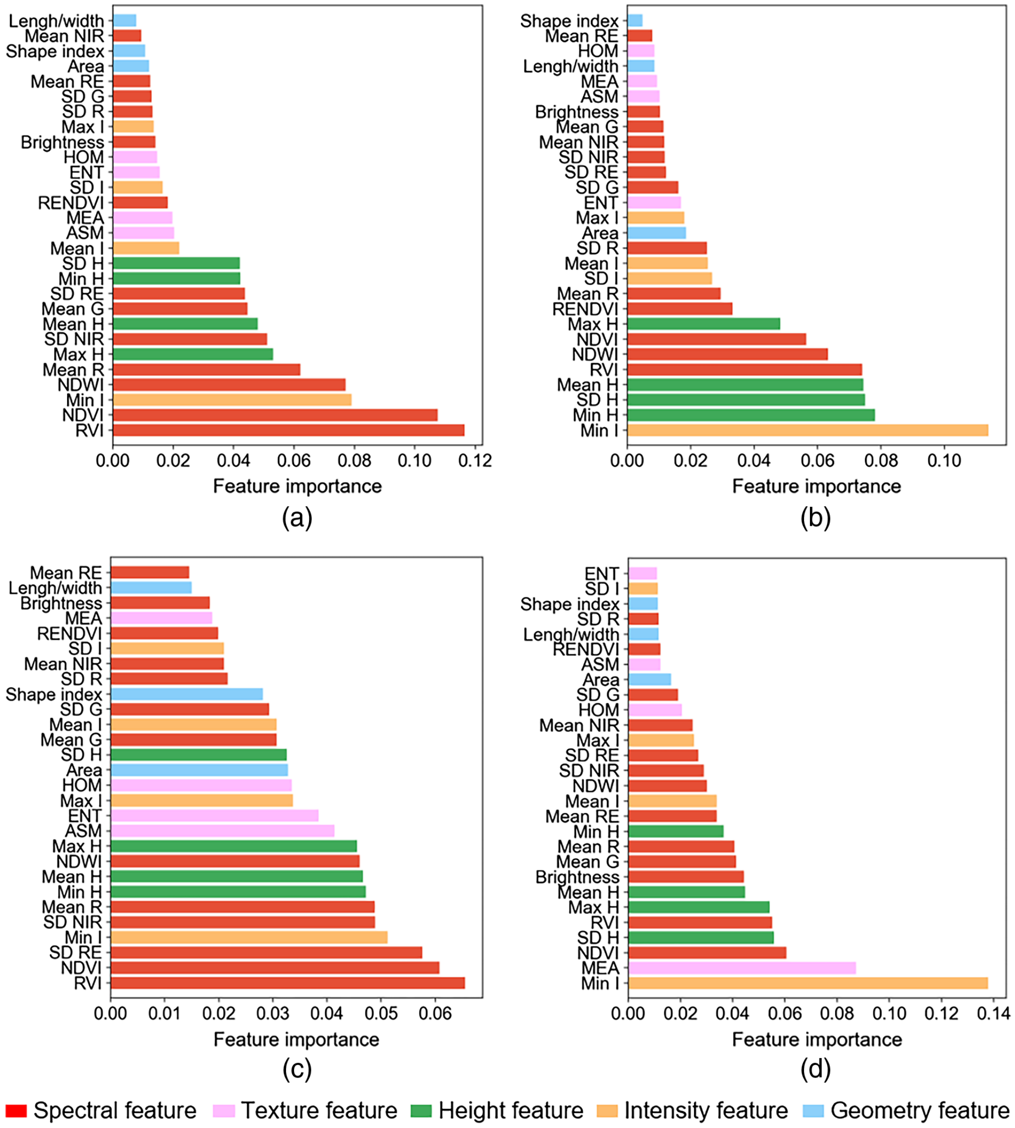

Fig. 7 Importance of different features to the green cover classification: (a) all classes, (b) tree, (c) shrub, and (d) grass.

PA (mean of 67%) are lower in all feature groups. In addition, the inclusion of height and IFs does not lead to significant differences in UA and PA for non-green cover.

We also analyzed the differences of $F1$-scores for each class across six feature groups [Fig. 9(b)], and Fig. 10 shows the confusion matrices that indicated further details of classification accuracy for the four classes. The $F1$-score of each class in the feature groups can be seen here except for the feature group G4: non-green cover > tree > grass > shrub. In the best performing feature group G6, three green cover classes are classified the most accurately, especially, the $F1$-score of the tree exceeds 0.9, while the non-green cover class have lower $F1$-score. The next is G5, with an average $F1$-score of 0.86 for each category. The G2 displays similar class recognition ability to G3 (average $F1$-scores 0.85 and 0.84, respectively), and some confusions also occur among the three green cover classes [Figs. 10(b) and 10(c)]. The poor performances are obtained by the feature groups G1 and G4 (both average $F1$-scores below 0.8), where slightly high $F1$-score of green cover is achieved using G4 since the shrub is frequently misclassified as tree or grass in G1 [Fig. 10(a)].

Further, in order to analyze the changes of $F1$-score for each green cover class after the inclusion of height or IF, we compared the difference of $F1$-score values between G1 (baseline) and the other four feature groups [Fig. 9(c)]. Similar trends of accuracy improvement with the

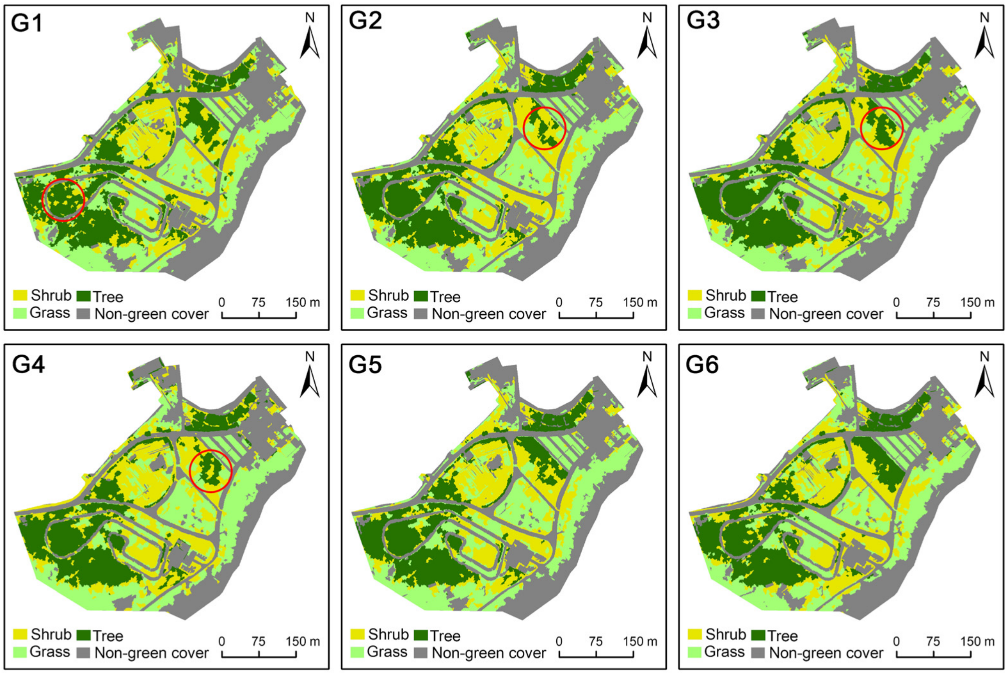

Fig. 8 Green cover map produced by different feature groups.

Table 8 Classification accuracy comparison of six feature groups. Bold indicates the best result.

Accuracy	G1	G2	G3	G4	G5	G6
OA (%)	78	85	83.5	81	86	**88.5**
OD (%)	25	**17**	18.5	33.5	**17**	18.5

additional features input can be observed: no classes are classified with lower $F1$-score compared to the baseline feature group. The highest increase is observed with shrub (exceeding 0.1), followed by tree, grass, and non-green cover. Moreover, for green cover classification, the role of HFs appear to be greater than that of IFs (G2 versus G3), and feature optimization also has a significant positive impact on the $F1$-score increase (G5 versus G6).

According to McNeamr's test (Table 9), significant statistical differences are seen between G1 and other feature groups except G4. M1 and G6 are the most significantly different, followed by G5, G2, and G3. However, G2 and G3, G2 and G5, G2 and G6 show no significant differences, as well as G5 and G6. Similarly, G3 show a similar pattern as G2. These results reveal that the addition of height and IFs do improve the classification accuracy, whereas the differences between two types of features are not significant. Meanwhile, only relying on increasing the amount of feature types appear to be ineffectual for improving the accuracy when the classification accuracy achieves a certain level.

4.4 *Classification Uncertainty*

The uncertainty maps of six feature groups based on the ensemble analysis are shown in Fig. 11. We classified the uncertainty of the final category for an object into three levels: low (L), moderate (M), and high (H). Specifically, if the votes of three classifiers are the same for an input image object, a complete agreement is obtained (L); if only two classifiers vote for the same class, a partial agreement is obtained (M); if three votes are completely different, no agreement is obtained (H).

It can be observed that the feature groups based on multispectral image and LiDAR data yield more objects with low uncertainty compared to those based on single data. Specifically, the best result is achieved by G6, with the largest number of low-uncertainty objects (82%), followed by

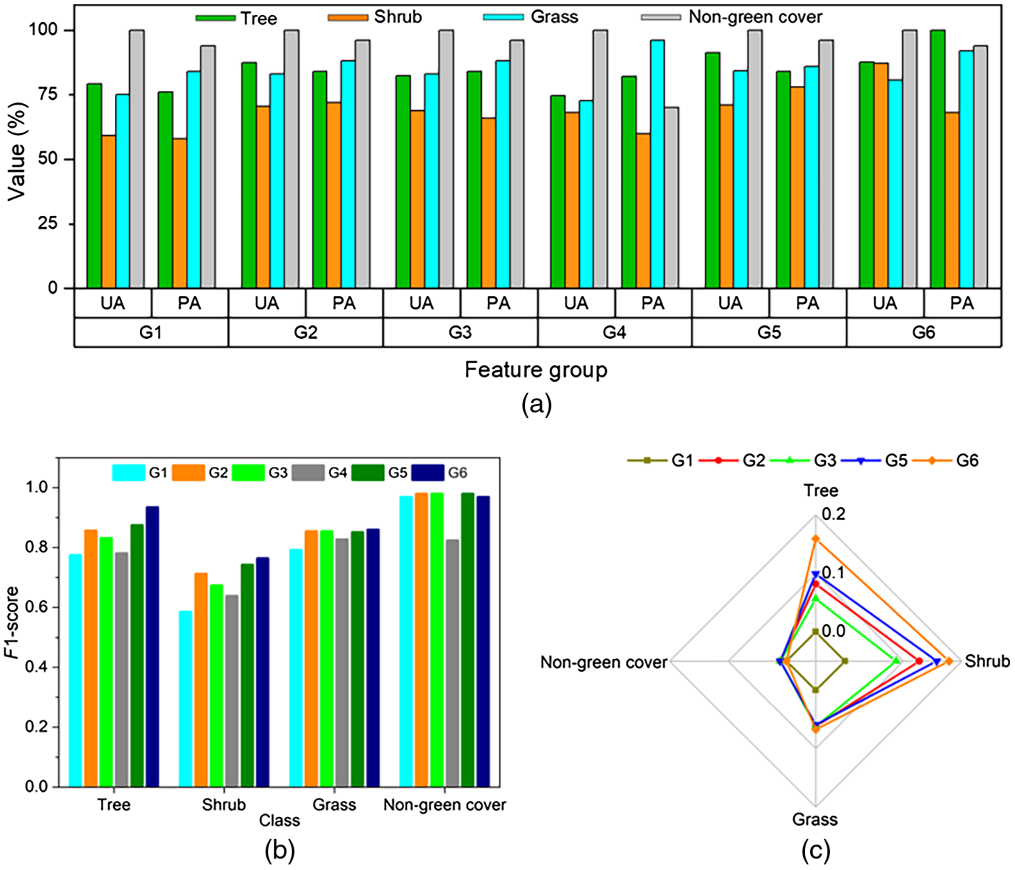

Fig. 9 (a) UA and PA, (b) *F*1-scores, and (c) changes in *F*1-scores of each class for different feature groups.

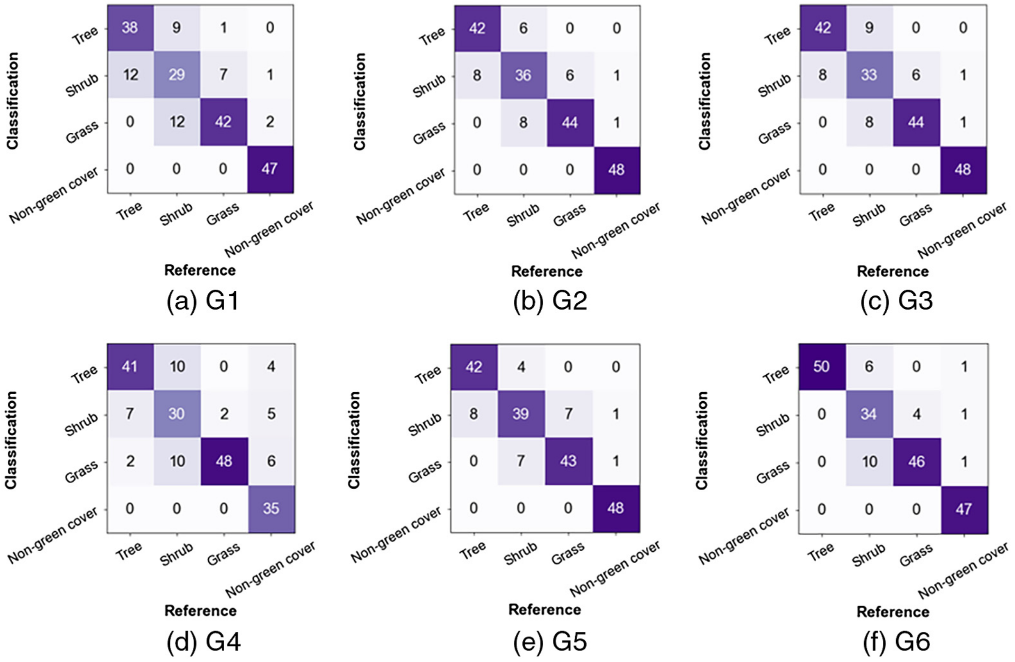

(a) G1

Classification \ Reference	Tree	Shrub	Grass	Non-green cover
Tree	38	9	1	0
Shrub	12	29	7	1
Grass	0	12	42	2
Non-green cover	0	0	0	47

(b) G2

Classification \ Reference	Tree	Shrub	Grass	Non-green cover
Tree	42	6	0	0
Shrub	8	36	6	1
Grass	0	8	44	1
Non-green cover	0	0	0	48

(c) G3

Classification \ Reference	Tree	Shrub	Grass	Non-green cover
Tree	42	9	0	0
Shrub	8	33	6	1
Grass	0	8	44	1
Non-green cover	0	0	0	48

(d) G4

Classification \ Reference	Tree	Shrub	Grass	Non-green cover
Tree	41	10	0	4
Shrub	7	30	2	5
Grass	2	10	48	6
Non-green cover	0	0	0	35

(e) G5

Classification \ Reference	Tree	Shrub	Grass	Non-green cover
Tree	42	4	0	0
Shrub	8	39	7	1
Grass	0	7	43	1
Non-green cover	0	0	0	48

(f) G6

Classification \ Reference	Tree	Shrub	Grass	Non-green cover
Tree	50	6	0	1
Shrub	0	34	4	1
Grass	0	10	46	1
Non-green cover	0	0	0	47

Fig. 10 Confusion matrices (validation objects) of green cover classification results based on six feature groups (a) G1, (b) G2, (c) G3, (d) G4, (e) G5, and (f) G1.

Table 9 Statistical significance difference between the six feature groups. Statistic values are on the left side of the diagonal (* indicates significant difference), while *p*-values on the right side.

	G1	G2	G3	G4	G5	G6
G1		8.91*	7.12*	0.7	10.67*	12.6*
G2	0.006		0.82	5.12*	1.3	1.44
G3	0.015	0.549		4.31*	1.67	1.57
G4	0.48	0.034	0.003		6.75*	12.3*
G5	0.002	0.773	0.302	0.014		0.64
G6	0.001	0.23	0.089	0.001	0.424	

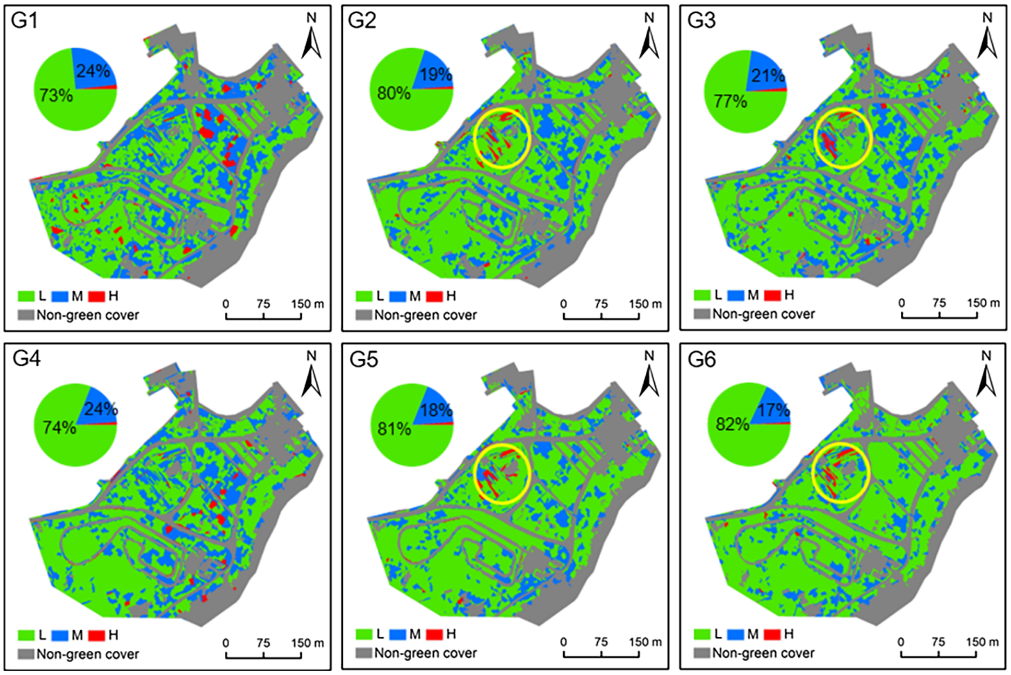

Fig. 11 Uncertainty map based on ensemble analysis of three classifiers.

G5 containing all features and G2, except for IFs, which acquire low-uncertainty objects of 81% and 80%, respectively. However, the feature groups G1, G3, and G4 had relatively poor performances, and their number of low-uncertainty objects are smaller than 80%. The high-uncertainty objects of G1 occur most frequently in the natural protection forest, mainly due to the capability of recognizing green cover being limited in the complex areas using only multispectral data. The high-uncertainty results for G4 mainly appear in the grass class. Furthermore, the uncertainty maps for all feature groups show high uncertainty for some shrubs in production nursery, apart from G1 and G4 (yellow circles).

5 Discussion

5.1 *Effects of Image Segmentation, Feature Selection, and Classification Method*

In addition to the input data, the selection of segmentation scheme, feature sets, and classification methods all play significant roles in improving object-based island green cover classification

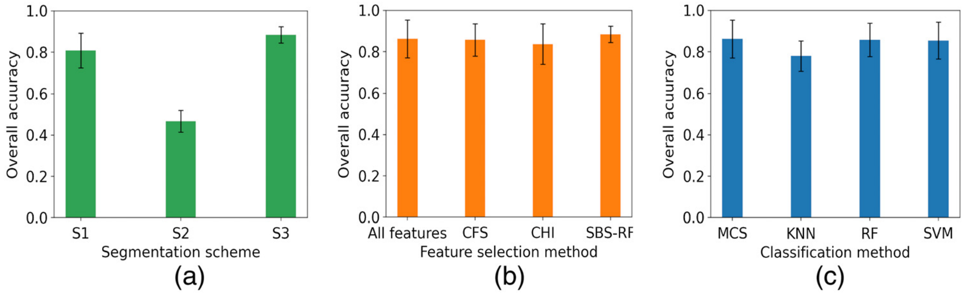

Fig. 12 Comparison of (a) different segmentation schemes, (b) feature selection methods, and (c) classification methods on OA of green cover classification. Columns denote mean of OA from five iterations, and lines denote standard deviation.

results. In the light of this, we further analyzed the impacts of these three factors on OA of green cover mapping.

As shown in Fig. 12(a), the green cover classification based on segmentation using both multispectral image and LiDAR data leads to higher OA when compared to those using either multispectral image or LiDAR data. Image segmentation including height and intensity information (S3) significantly improve classification accuracy, with OA increasing by 7.7% and 34%, respectively, when compared to those using single data alone (S1 or S2). Regarding the influence of different feature selection methods on OA [Fig. 12(b)], higher OA (2%) is achieved using the feature set selected by SBS-RF method than using all the candidate features, whereas the other two methods show no positive effects on OA. Classification using an MCS is superior to a single classifier [Fig. 12(c)], with OA increasing by 0.5% (RF), 0.8% (SVM), and 8.2% (KNN), respectively.

As discussed above, an appropriate selection of segmentation scheme, classification method, and feature selection method are of great significance to the improvement of green cover classification accuracy, in which the impact of feature selection is smaller than the other two factors.

5.2 *Potential of Integrating Multispectral Image and LiDAR Data for Island Green Cover Mapping*

In this study, six feature groups were adopted to incorporate the advantages of different feature sets, which are summarized in Table 5. As expected, the island green cover classification accuracy increased with the information input into the classification process. The results show that the integration of multispectral image and LiDAR data provided a significant improvement for classification accuracy, with OA increasing by 10.5% and 7.5%, and with OD decreasing by 8% and 16.5%, respectively, when compared to those using multispectral image or LiDAR data alone. It can also be found that the HFs derived from LiDAR data appear to be more important in island green cover classification, higher OA of 1.5% and lower OD of 1.5% are obtained than the IFs, which agree with the findings of the previous studies.[26,35]

When exploring the potential of these two datasets, their performance for per-green cover class recognition is worth mentioning. The accuracy of each green cover class is in consistent with the trend of OA, i.e., including more information in the mapping can improve the $F1$-score of class. The results indicate that the improvement is more significant for shrub and tree using both multispectral image and LiDAR data, with $F1$-score increasing by 0.17 and 0.15, respectively. For the recognition of grass, the role of height and IFs are interchangeable, where either feature type can increase the $F1$-score by 0.06. However, combining multispectral image and LiDAR data barely affected the accuracy of non-green cover class (across all feature groups).

Another benefit is that the integration of these two complementary data can reduce classification uncertainty. The value of classification uncertainty presents some differences among the six feature groups. Using all the candidate features (G5) appears to generate a larger proportion of correctly classified objects with lower uncertainty when compared to other feature groups (G1, G2, G3, and G4). In particular, some shrubs in the production nursery have high uncertainty except for the feature groups G1 and G4. A reasonable explanation is that the multispectral image acquisition time is a year later than LiDAR data and changes in green cover were occurred over this time.

Although integrating UAV-acquired multispectral image and LiDAR data is regarded as an effective way for island green cover mapping, there are still some aspects worth considering. For example, in data preprocessing, the selection of interpolation techniques for producing the intensity image, the unidentified effects of laser beam incident angles, and the energy loss due to narrow scan angle, may affect the classification accuracy. Utilizing more beneficial three-dimensional features derived from LiDAR data to further improve the classification results, and the performance of a detailed green cover mapping is expected to be explored. In addition, the applicability of UAV data acquired over large island areas remains a challenge owing to the limited endurance of the UAV.

6 Conclusion

In this study, an effective object-based island green cover mapping was proposed using both UAV-acquired multispectral image and LiDAR data. According to the results, three conclusions can be drawn as follows.

(1) The inclusion of height and intensity information derived from LiDAR data into the image segmentation process can effectively reduce the number of mixed objects and make the segments more consistent with the ground green cover objects.
(2) Using multiple features types can yield a significant improvement for classification accuracy (OA increased by 3.5% to 10.5% and OD decreased by 1.5% to 16.5%) as well as reduce the uncertainty of classification (reduced by 2% to 9%). Moreover, the improvement is more significant for shrub and tree when compared to grass class.
(3) In terms of feature importance, overall, SFs play a dominant role in green cover classification, followed by height, intensity, texture, and geometry features. However, the feature importance of per-class differed to a great extent, where the contribution of height and IFs were stable for per-class, with ranking in the top 15.

Acknowledgments

This study was funded by the National Natural Science Foundation of China (Grant Nos. 41871235 and 42071297) and the Fundamental Research Funds for the Central Universities (Grant No. 020914380080). The authors declare no potential conflict of interest.

References

1. S. Gao et al., "Dynamic assessment of island ecological environment sustainability under urbanization based on rough set, synthetic index and catastrophe progression analysis theories," *Ocean Coast. Manage.* **178**, 104790 (2019).
2. S. Roy, J. Byrne, and C. Pickering, "A systematic quantitative review of urban tree benefits, costs, and assessment methods across cities in different climatic zones," *Urban For. Urban Gree.* **11**(4), 351–363 (2012).
3. H. Gu, A. Singh, and P. A. Townsend, "Detection of gradients of forest composition in an urban area using imaging spectroscopy," *Remote Sens. Environ.* **167**, 168–180 (2015).
4. R. Gini et al., "Use of unmanned aerial systems for multispectral survey and tree classification: a test in a park area of northern Italy," *Eur. J. Remote Sens.* **47**, 251–269 (2014).
5. J. Komárek, T. Klouček, and J. Prošek, "The potential of unmanned aerial systems: a tool towards precision classification of hard-to-distinguish vegetation types?" *Int. J. Appl. Earth Obs.* **71**, 9–19 (2018).
6. H. Liang et al., "Using unmanned aerial vehicle data to assess the three-dimension green quantity of urban green space: a case study in Shanghai, China," *Landscape Urban Plan.* **164**, 81–90 (2017).

7. A. C. Watts, V. G. Ambrosia, and E. A. Hinkley, "Unmanned aircraft systems in remote sensing and scientific research: classification and considerations of use," *Remote Sensors-Basel* **4**(6), 1671–1692 (2012).
8. E. Marris, "Drones in science: fly, and bring me data," *Nature* **498**(7453), 156 (2013).
9. O. S. Ahmed et al., "Hierarchical land cover and vegetation classification using multispectral data acquired from an unmanned aerial vehicle," *Int. J. Remote Sens.* **38**(8-10), 2037–2052 (2017).
10. B. Lu and Y. He, "Optimal spatial resolution of unmanned aerial vehicle (UAV)-acquired imagery for species classification in a heterogeneous grassland ecosystem," *Gisci. Remote Sens.* **55**(2), 205–220 (2018).
11. N. Miura et al., "Herbaceous vegetation height map on Riverdike derived from UAV LiDAR data," in *IEEE Int. Geosci. and Remote Sens. Symp. (IGARSS 2018)*, pp. 5469–5472 (2018).
12. S. M. Hamylton et al., "Evaluating techniques for mapping island vegetation from unmanned aerial vehicle (UAV) images: pixel classification, visual interpretation and machine learning approaches," *Int. J. Appl. Earth Obs.* **89**, 102085 (2020).
13. J. P. Ardila et al., "Context-sensitive extraction of tree crown objects in urban areas using VHR satellite images," *Int. J. Appl. Earth Obs.* **15**, 57–69 (2012).
14. W. Yin and J. Yang, "Sub-pixel vs. super-pixel-based greenspace mapping along the urban-rural gradient using high spatial resolution Gaofen-2 satellite imagery: a case study of Haidian District, Beijing, China," *Int. J. Remote Sens.* **38**(22), 6386–6406 (2017).
15. X. Zhang, X. Feng, and H. Jiang, "Object-oriented method for urban vegetation mapping using IKONOS imagery," *Int. J. Remote Sens.* **31**(1), 177–196 (2010).
16. K. N. Youngentob et al., "Mapping two Eucalyptus subgenera using multiple endmember spectral mixture analysis and continuum-removed imaging spectrometry data," *Remote Sens. Environ.* **115**(5), 1115–1128 (2011).
17. N. Goodwin, R. Turner, and R. Merton, "Classifying Eucalyptus forests with high spatial and spectral resolution imagery: AN investigation of individual species and vegetation communities," *Aust. J. Bot.* **53**(4), 337–345 (2005).
18. W. Zhou et al., "Object-based land cover classification of shaded areas in high spatial resolution imagery of urban areas: a comparison study," *Remote Sens. Environ.* **113**(8), 1769–1777 (2009).
19. A. O. Onojeghuo and A. R. Onojeghuo, "Object-based habitat mapping using very high spatial resolution multispectral and hyperspectral imagery with LiDAR data," *Int. J. Appl. Earth Obs.* **59**, 79–91 (2017).
20. Y. Huang et al., "Toward automatic estimation of urban green volume using airborne LiDAR data and high resolution remote sensing images," *Front. Earth Sci.-PRC* **7**(1), 43–54 (2013).
21. S. Kim et al., "Tree species differentiation using intensity data derived from leaf-on and leaf-off airborne laser scanner data," *Remote Sens. Environ.* **113**(8), 1575–1586 (2009).
22. W. Y. Yan, A. Shaker, and N. El-Ashmawy, "Urban land cover classification using airborne LiDAR data: a review," *Remote Sens. Environ.* **158**, 295–310 (2015).
23. D. Lu et al., "A survey of remote sensing-based aboveground biomass estimation methods in forest ecosystems," *Int. J. Digit. Earth* **9**(1), 63–105 (2014).
24. J. Im, J. R. Jensen, and M. E. Hodgson, "Object-based land cover classification using high-posting-density LiDAR data," *GISci. Remote Sens.* **45**(2), 209–228 (2013).
25. R. Pu and S. Landry, "A comparative analysis of high spatial resolution IKONOS and WorldView-2 imagery for mapping urban tree species," *Remote Sens. Environ.* **124**, 516–533 (2012).
26. M. Alonzo, B. Bookhagen, and D. A. Roberts, "Urban tree species mapping using hyperspectral and lidar data fusion," *Remote Sens. Environ.* **148**, 70–83 (2014).
27. S. W. Myint et al., "Per-pixel vs. object-based classification of urban land cover extraction using high spatial resolution imagery," *Remote Sens. Environ.* **115**(5), 1145–1161 (2011).
28. J. Liu, P. Li, and X. Wang, "A new segmentation method for very high resolution imagery using spectral and morphological information," *ISPRS J. Photogramm. Remote Sens.* **101**, 145–162 (2015).
29. T. Blaschke, "Object based image analysis for remote sensing," *ISPRS J. Photogramm. Remote Sens.* **65**(1), 2–16 (2010).

30. Z. Zhang et al., "Object-based tree species classification in urban ecosystems using LiDAR and hyperspectral data," *Forests* **7**(12), 122 (2016).
31. Y. Ke, L. J. Quackenbush, and J. Im, "Synergistic use of QuickBird multispectral imagery and LIDAR data for object-based forest species classification," *Remote Sens. Environ.* **114**(6), 1141–1154 (2010).
32. C. B. Kukunda et al., "Ensemble classification of individual Pinus crowns from multispectral satellite imagery and airborne LiDAR," *Int. J. Appl. Earth Obs.* **65**, 12–23 (2018).
33. W. Liang et al., "Mapping vegetation at species level with high-resolution multispectral and lidar data over a large spatial area: a case study with Kudzu," *Remote Sens.-Basel* **12**(4), 609 (2020).
34. R. Pu and S. Landry, "Mapping urban tree species by integrating multi-seasonal high resolution pléiades satellite imagery with airborne LiDAR data," *Urban For. Urban Gree.* **53**, 126675 (2020).
35. L. Liu et al., "Mapping urban tree species using integrated airborne hyperspectral and LiDAR remote sensing data," *Remote Sens. Environ.* **200**, 170–182 (2017).
36. P. Du et al., "Multiple classifier system for remote sensing image classification: a review," *Sensors-Basel* **12**(4), 4764–4792 (2012).
37. J. Wu, W. Yao, and P. Polewski, "Mapping individual tree species and vitality along urban road corridors with LiDAR and imaging sensors: point density versus view perspective," *Remote Sens.-Basel* **10**(9), 1403 (2018).
38. M. A. Hall and G. Holmes, "Benchmarking attribute selection techniques for discrete class data mining," *IEEE Trans. Knowl. Data Eng.* **15**(6), 1437–1447 (2003).
39. J. Chen et al., "Mapping urban land cover of a large area using multiple sensors multiple features," *Remote Sens.-Basel* **10**(6), 872 (2018).
40. C. Zhang, "Combining hyperspectral and lidar data for vegetation mapping in the Florida Everglades," *Photogramm. Eng. Remote Sens.* **80**(8), 733–743 (2014).
41. U. Vepakomma, B. St-Onge, and D. Kneeshaw, "Spatially explicit characterization of boreal forest gap dynamics using multi-temporal lidar data," *Remote Sens. Environ.* **112**(5), 2326–2340 (2008).
42. J. Adamczyk, "The effect of scaling methods on the calculation of environmental indices," *Ecol. Quest.* **17**, 9 (2013).
43. M. Baätz and A. Schape, "Multiresolution segmentation: an optimization approach for high quality multi-scale image segmentation," in *Angewandte Geographische Informations-Verarbeitung, XII*, J. Strobl, T. Blaschke, and G. Griesbner, Eds., pp. 12–23, Wichmann Verlag, Karlsruhe (2000).
44. H. Huang, *Scale Issues in Object-Oriented Image Analysis*, Institute of Remote Sensing Applications, Chinese Academy of Sciences (2003).
45. Q. Wu et al., "Land-cover classification using GF-2 images and airborne lidar data based on random forest," *Int. J. Remote Sens.* **40**(5–6), 2410–2426 (2019).
46. H. Liu et al., "Object-based island hierarchical land cover classification using unmanned aerial vehicle multitype data," *J. Appl. Remote Sens.* **14**(3), 034514 (2020).
47. C. Cheadle et al., "Analysis of microarray data using Z score transformation," *J. Mol. Diagn.* **5**(2), 73–81 (2003).
48. L. Bruzzone and F. Roli, "An extension of the Jeffreys–Matusita distance to multiclass cases for feature selection," *IEEE Trans. Geosci. Remote Sens.* **33**(6), 1318–1321 (1995).
49. H. Liu and R. Setiono, "Chi2: feature selection and discretization of numeric attributes," in *Proc. Int. Conf. Tools with Artif. Intell.*, pp. 388–391 (1995).
50. M. A. Hall, *Correlation-Based Feature Selection for Discrete and Numeric Class Machine Learning*, University of Waikato, Hamilton (2000).
51. T. M. Phuong, Z. Lin, and R. B. Altman, "Choosing SNPs using feature selection," in *Proc. IEEE Comput. Syst. Bioinf. Conf.*, pp. 301–309 (2005).
52. G. Chen et al., "Geographic object-based image analysis (GEOBIA): emerging trends and future opportunities," *Gisci. Remote Sens.* **55**(2), 159–182 (2018).
53. L. Ma et al., "Training set size, scale, and features in geographic object-based image analysis of very high resolution unmanned aerial vehicle imagery," *ISPRS J. Photogramm. Remote Sens.* **102**, 14–27 (2015).

54. L. Breiman, “Random forests,” *Mach. Learn.* **45**(1), 5–32 (2001).
55. C. Sothe et al., “Tree species classification in a highly diverse subtropical forest integrating UAV-based photogrammetric point cloud and hyperspectral data,” *Remote Sens.-Basel* **11**(11), 1338 (2019).
56. I. Fernandez Luque et al., “Non-parametric object-based approaches to carry out ISA classification from archival aerial orthoimages,” *IEEE J.-Stars* **6**(4), 2058–2071 (2013).
57. R. G. Pontius and M. Millones, “Death to kappa: birth of quantity disagreement and allocation disagreement for accuracy assessment,” *Int. J. Remote Sens.* **32**(15), 4407–4429 (2011).
58. R. G. Congalton, “A review of assessing the accuracy of classifications of remotely sensed data,” *Remote Sens. Environ.* **37**(1), 35–46 (1991).
59. A. Agresti, “Categorical data analysis,” *Publ. Am. Stat. Assoc.*, Vol. 482, John Wiley & Sons (2003).

Hao Liu received his BS degree in geomatics engineering from the Central South University of Forestry and Technology, Changsha, China, in 2017 and his MS degree in photogrammetry and remote sensing from Nanjing University, Nanjing, China, in 2020. He is currently pursuing his PhD in cartography and geographical information system at the same university. His research topics are remote sensing, land cover, and machine learning.

Pengfeng Xiao received his BM degree in land resource management from Hunan Normal University, Changsha, China, in 2002 and his PhD in cartography and geographical information systems from Nanjing University, Nanjing, China, in 2007. He is currently a professor in the Department of Geographic Information Science at Nanjing University. His research interests include high-resolution remote sensing image analysis, remote sensing of snow cover, and land-use and land-cover change.

Xueliang Zhang received his BS degree in geographical information system and his PhD in remote sensing of resources and environment from Nanjing University, Nanjing, China, in 2010 and 2015, respectively. He is currently an associate professor in the Department of Geographic Information Science at Nanjing University. His research interests include high-resolution remote sensing image analysis, semantic segmentation, and deep learning for remote sensing.

Xinghua Zhou is currently a professor of the First Institute of Oceanography, Ministry of Natural Resources. His research interests include marine surveying and charting.

Jie Li is currently a doctor of the First Institute of Oceanography, Ministry of Natural Resources. His research interests include UAV remote sensing and marine surveying and charting.

Rui Guo received her BS degree in geographic information science from Nanjing Normal University, Nanjing, China, in 2019. She is currently pursuing her MS degree in cartography and geographical information system at Nanjing University, Nanjing, China. Her research interests include deep learning for remote sensing and land cover change.